

Polymorphous Exhibitions of Iron(III) Oxide during Isothermal Oxidative Decompositions of Iron Salts: A Key Role of the Powder Layer Thickness

Martin Hermanek and Radek Zboril*

Centre for Nanomaterial Research, Palacky University, Slechtitelu 11, 783 71 Olomouc, Czech Republic, and Departments of Experimental Physics and Physical Chemistry, Palacky University, Svobody 26, 771 46 Olomouc, Czech Republic

Received April 30, 2008. Revised Manuscript Received June 11, 2008

Thermal decomposition of iron(II) oxalate dihydrate, $\text{FeC}_2\text{O}_4 \cdot 2\text{H}_2\text{O}$, was studied under isothermal conditions in air by using of X-ray diffraction (XRD), transmission electron microscopy (TEM), magnetic measurements, and Mössbauer spectroscopy. Direct in situ monitoring of sample temperature was found to be a breaking point in understanding the decomposition mechanism resulting in different polymorphous product compositions which are simultaneously dependent on the powder layer thickness and reaction temperature. At a certain temperature, there exists a critical sample layer thickness (weight, m_c), below which the optimal oxygen access into the whole powder volume is enabled and the reaction proceeds under truly isothermal conditions. In such a case hematite ($\alpha\text{-Fe}_2\text{O}_3$) is the only crystalline decomposition product. Above m_c , at worsened diffusion conditions, a dramatic time-limited increase in the sample temperature has been observed. The appearance of such an “exoeffect” is a consequence of the violent diffusion of air oxygen inside the sample volume which depends precisely on the layer thickness and set temperature. During this exothermal stage of the reaction process the changes in kinetics and mechanism of decomposition are evidenced by an abrupt fall in the oxalate content and by the formation of the vacant structure of maghemite ($\gamma\text{-Fe}_2\text{O}_3$). The generalization of these phenomena has been demonstrated by several examples of oxidative decompositions of other metal salts, where the analogous exoeffect has been detected and various polymorphous mixtures containing α -, β -, γ -, and/or amorphous Fe_2O_3 have been identified among the reaction products. Our findings explain unambiguously the literature discrepancies concerning the different phase compositions of samples prepared by the “isothermal” solid-state decomposition processes. What is more, when the key reaction parameters are precisely controlled, single-phase nanocrystalline products possessing superior properties can be obtained.

1. Introduction

Iron(III) oxide represents an exemplary polymorphic compound yielding several crystal structures depending on the synthetic procedure and/or on the geophysical and geochemical conditions at which it is formed in nature.^{1,2} In the nanocrystalline state, all polymorphs reveal some unique properties exploitable in various fields of modern nanotechnologies. The thermodynamically stable hexagonal $\alpha\text{-Fe}_2\text{O}_3$ phase (hematite), in the form of nanoparticles, is an exceedingly efficient catalyst in many processes of heterogeneous catalysis^{3–6} and also a very promising candidate for photocatalytic splitting of water and other

compounds.^{7–9} Sensors made of the $\alpha\text{-Fe}_2\text{O}_3$ nanoparticles exhibit great sensitivity in various biosensing and gas-sensing applications.^{10,11} The three-dimensional flower-like hematite nanostructures are well applicable in water treatment technologies as they show an exceptional ability to remove various pollutants from water.¹² From the geophysical viewpoint, hematite nanolamellas are responsible for the intense magnetism in the hematite-ilmenite systems known as Martian magnetic anomalies.^{13,14} The second most frequent polymorph, cubic spinel $\gamma\text{-Fe}_2\text{O}_3$ (maghemite), is extensively used in biomedical nanotechnologies. Thanks to

* Corresponding author. E-mail: zboril@prfnw.upol.cz.

- (1) Zboril, R.; Mashlan, M.; Petridis, D. *Chem. Mater.* **2002**, *14*, 969–982.
- (2) Cornell, R. M.; Schwertmann, U. *The Iron Oxides*; VCH: Weinheim, Germany, 1996.
- (3) Shin, E. J.; Miser, D. E.; Chan, W. G.; Hajaligol, M. R. *Appl. Catal., B* **2005**, *61*, 79–89.
- (4) Jung, H.; Park, H.; Kim, J.; Lee, J. H.; Hur, H. G.; Myung, N. V.; Choi, H. *Environ. Sci. Technol.* **2007**, *41*, 4741–4747.
- (5) Zhong, Z.; Ho, J.; Teo, J.; Shen, S.; Gedanken, A. *Chem. Mater.* **2007**, *19*, 4776–4782.
- (6) Kastner, J. R.; Ganagavaram, R.; Kolar, P.; Teja, A.; Xu, C. *Environ. Sci. Technol.* **2008**, *42*, 556–562.

(7) Cesar, I.; Kay, A.; Martinez, J.; Gratzel, M. *J. Am. Chem. Soc.* **2006**, *128*, 4582–4583.

(8) Kay, A.; Cesar, I.; Gratzel, M. *J. Am. Chem. Soc.* **2006**, *128*, 15714–15721.

(9) Apte, S. K.; Naik, S. D.; Sonawane, R. S.; Kale, B. B. *J. Am. Ceram. Soc.* **2007**, *90*, 412–414.

(10) Hu, X. L.; Yu, J. C.; Gong, J. M.; Li, Q.; Li, G. S. *Adv. Mater.* **2007**, *19*, 2324–2329.

(11) Choi, W. S.; Koo, H. Y.; Zhongbin, Z.; Li, Y. D.; Kim, D. Y. *Adv. Funct. Mater.* **2007**, *17*, 1743–1749.

(12) Zhong, L. S.; Hu, J. S.; Liang, H. P.; Cao, A. M.; Song, W. G.; Wan, L. J. *Adv. Mater.* **2006**, *18*, 2426–2431.

(13) Robinson, P.; Harrison, R. J.; McEnroe, S. A.; Hargraves, R. B. *Nature* **2002**, *418*, 517–520.

(14) McEnroe, S. A.; Carter-Stiglitz, B.; Harrison, R. J.; Robinson, P.; Fabian, K.; McCammon, C. *Nat. Nanotechnol.* **2007**, *2*, 631–634.

the combination of suitable magnetic (ferrimagnetic, superparamagnetic) properties and ultrasmall particle dimensions, functionalized maghemite and/or magnetite (Fe_3O_4) nanoparticles represent key materials for MRI (magnetic resonance imaging) contrast enhancement, tomographic imaging, targeted drug delivery, anticancer therapy in hyperthermia techniques, and cell labeling and separation.^{15–19} Orthorhombic $\epsilon\text{-Fe}_2\text{O}_3$ has been prepared almost exclusively as rodlike nanoparticles exhibiting a giant coercive force of 2 T at room temperature.^{20–25} This force most likely results from the combination of large magnetocrystalline and shape anisotropies, small saturation magnetization, and the single-domain character of particles. Being the highest coercivity so far reported in any metal oxide-based material makes this polymorph very promising in the development of a new generation of magnetic recording media. The last and rarest structural form is the cubic $\beta\text{-Fe}_2\text{O}_3$ phase possessing, as the only structure among all polymorphs, paramagnetic behavior at room temperature.^{1,26} Nevertheless, if synthesized by chemical vapor condensation technique, it creates unique hollow nanoparticles composed of several shells with a thickness of 3–5 nm.²⁷ Recent data indicate that such unique hollow nanostructures can be thermally transformed to maghemite.²⁸ The preservation of this remarkable morphology of particles during polymorphic transition could result in further improvement of exceptional magnetic properties of nanomaghemite. In addition to the four mentioned polymorphs, there are several synthetic routes toward the amorphous iron(III) oxide phase yielding ultrasmall nondiffracting particles with a nonperiodic lattice.²⁹ They can be utilized as superior catalysts and, in the form of nanocomposites with SiO_2 and Au, as very efficient magneto-optical and humidity sensors, respectively.^{29–31}

Such extraordinary application potential of all nanocrystalline iron(III) oxides has induced extensive development of new synthetic routes toward nanoparticles of required

structure and morphology. Among them, thermal decomposition of suitable Fe precursors in solutions (pyrolysis) represents probably the most sophisticated synthetic procedure as it leads to monodispersed nanoparticles possessing defined structure and morphology depending on reaction conditions.^{4,32–37} Iron pentacarbonyl, iron–oleate complex, and iron carboxylate salts are the most frequent precursors used for this synthetic technique.

However, preparations based exclusively on the thermally induced oxidative decompositions of suitable Fe-bearing precursors in a solid state also exist. The simplicity, cost effectiveness, and possibility of large-scale production are the key advantages of these “precursor syntheses” from the technological point of view. Moreover, truly monodispersed systems with a controlled particle size can be achieved by direct solid-state procedures as proved in the case of nanocrystalline iron oxides prepared from iron oleate.³⁸ Another considerable advantage of precursor syntheses is the preservation of precursor phase morphology in the metal oxide nanophase, which can be demonstrated by tailored decompositions of polyols-based metal alkoxides.³⁹ One-step synthesis and functionalization of magnetic iron(III) oxide phase, when decomposition proceeds in the presence of a coating agent, is another remarkable aspect of the solid-state syntheses. Such core–shell nanoparticles of maghemite capped with palmitic acid can be produced from iron nitrate precursor at mild thermal conditions.⁴⁰

In some cases, iron(III) oxide nanostructures possessing superior properties unattainable by wet chemical routes can be prepared using *oxidative solid-state decomposition*. Amorphous iron(III) oxide nanopowder with the largest surface area (ca. 400 m^2/g) so far reported for nonsupported iron oxides has been successfully synthesized by thermal oxidation of the Prussian blue precursor.⁴¹ Iron(III) oxide and/or magnetite nano- and microstructures maintaining the unique peanut-like, ellipsoidal, or rodlike morphologies of the precursor can be prepared by the oxidative decomposition of iron(II) carbonate.⁴² An analogous preparation procedure was applied to produce rodlike nanoparticles of magnetite, hematite, and/or maghemite by thermally induced oxidative

(15) Andrä, W.; Nowak, H. *Magnetism in Medicine*; Wiley-VCH: Berlin, Germany, 1998.
 (16) Häfeli, U.; Schütt, W.; Teller, J.; Zboraski, M. *Scientific and Clinical Applications of Magnetic Carriers*; Plenum Press: New York, 1997.
 (17) Pankhurst, Q. A.; Connolly, J.; Jones, S. K.; Dobson, J. *J. Phys. D: Appl. Phys.* **2003**, *36*, R167–R181.
 (18) Gleich, B.; Weizenecker, R. *Nature* **2005**, *435*, 1214–1217.
 (19) Berret, J. F.; Schonbeck, N.; Gazeau, F.; El Kharrat, D.; Sandre, O.; Vacher, A.; Airiau, M. *J. Am. Chem. Soc.* **2006**, *128*, 1755–1761.
 (20) Jin, B.; Ohkoshi, S.; Hashimoto, K. *Adv. Mater.* **2004**, *16*, 48–51.
 (21) Popovici, M.; Gich, M.; Niznansky, D.; Roig, A.; Savii, C.; Casas, L.; Molins, E.; Zaveta, K.; Enache, C.; Sort, J.; de Brion, S.; Chouteau, G.; Nogues, J. *Chem. Mater.* **2004**, *16*, 5542–5548.
 (22) Jin, J.; Hashimoto, K.; Ohkoshi, S. *J. Mater. Chem.* **2005**, *15*, 1067–1071.
 (23) Kurmoo, M.; Rehspringer, J. L.; Hutlova, A.; D’Orleans, C.; Vilminot, S.; Estournes, C.; Niznansky, D. *Chem. Mater.* **2005**, *17*, 1106–1114.
 (24) Gich, M.; Frontera, C.; Roig, A.; Taboada, E.; Molins, E.; Rechenberg, H. R.; Ardisson, J. D.; Macedo, W.; Ritter, C.; Hardy, V.; Sort, J.; Skumryev, V.; Nogues, J. *Chem. Mater.* **2006**, *18*, 3889–3897.
 (25) Ding, Y.; Morber, J. R.; Snyder, R. L.; Wang, Z. L. *Adv. Funct. Mater.* **2007**, *17*, 1172–1178.
 (26) Kumar, A.; Singhal, A. *Nanotechnology* **2007**, *18*, 475703.
 (27) Lee, J. S.; Im, S. S.; Lee, C. W.; Yu, J. H.; Choa, Y. H.; Oh, S. T. *J. Nanopart. Res.* **2004**, *6*, 627–631.
 (28) Lee, C. W.; Jung, S. S.; Lee, J. S. *Mater. Lett.* **2008**, *62*, 561–563.
 (29) Machala, L.; Zboril, R.; Gedanken, A. *J. Phys. Chem. B* **2007**, *111*, 4003–4018.
 (30) Prabhakaran, K.; Shafi, K.; Ulman, A.; Ogino, T. *Adv. Mater.* **2001**, *13*, 1859–1862.
 (31) Neri, G.; Bonavita, A.; Milone, C.; Pistone, A.; Galvagno, S. *Sens. Actuators, B* **2003**, *92*, 326–330.

(32) Hyeon, T.; Lee, S. S.; Park, J.; Chung, Y.; Bin Na, H. *J. Am. Chem. Soc.* **2001**, *123*, 12798–12801.
 (33) Yu, W. W.; Falkner, J. C.; Yavuz, C. T.; Colvin, V. L. *Chem. Commun.* **2004**, 2306–2307.
 (34) Park, J.; Lee, E.; Hwang, N. M.; Kang, M. S.; Kim, S. C.; Hwang, Y.; Park, J. G.; Noh, H. J.; Kini, J. Y.; Park, J. H.; Hyeon, T. *Angew. Chem., Int. Ed.* **2005**, *44*, 2872–2877.
 (35) Cozzoli, P. D.; Snoeck, E.; Garcia, M. A.; Giannini, C.; Guagliardi, A.; Cervellino, A.; Gozzo, F.; Hernando, A.; Achterhold, K.; Ciobanu, N.; Parak, F. G.; Cingolani, R.; Manna, L. *Nano Lett.* **2006**, *6*, 1966–1972.
 (36) Roca, A. G.; Morales, M. P.; O’Grady, K.; Serna, C. J. *Nanotechnology* **2006**, *17*, 2783–2788.
 (37) Kwon, S. G.; Piao, Y.; Park, J.; Angappane, S.; Jo, Y.; Hwang, N. M.; Park, J. G.; Hyeon, T. *J. Am. Chem. Soc.* **2007**, *129*, 12571–12584.
 (38) Bronstein, L. M.; Huang, X. L.; Retrum, J.; Schmucker, A.; Pink, M.; Stein, B. D.; Dragnea, B. *Chem. Mater.* **2007**, *19*, 3624–3632.
 (39) Larcher, D.; Sudant, G.; Patrice, R.; Tarascon, J. M. *Chem. Mater.* **2003**, *15*, 3543–3551.
 (40) Zboril, R.; Bakandritsos, A.; Mashlan, M.; Tzitzios, V.; Dallas, P.; Trapalis, Ch.; Petridis, D. *Nanotechnology* **2008**, *19*, 095602.
 (41) Zboril, R.; Machala, L.; Mashlan, M.; Sharma, V. *Cryst. Growth Des.* **2004**, *4*, 1317–1325.
 (42) Xuan, S. H.; Hao, L. Y.; Jiang, W. Q.; Song, L.; Hu, Y.; Chen, Z. Y.; Fei, L. F.; Li, T. W. *Cryst. Growth Des.* **2007**, *7*, 430–434.

conversion of iron(II) oxalate dihydrate possessing the same rodlike morphology.⁴³ These “template precursor syntheses” generally exploiting the preservation of the advantageous size and morphology properties of the precursor phase could be the very promising synthetical ways leading toward iron oxide nanostructures with exceptional catalytic, sorption, and magnetic properties. Moreover, the applicability of this template-like approach increases if the precursor particles are suitably coated and the final iron oxide nanoparticles are prevented from sintering.⁴⁴ Among other examples, in our recent work, we prepared the hematite-based nanocatalyst with controlled crystallinity by thermal decomposition of iron(II) oxalate dihydrate.⁴⁵ This nanopowder revealed the highest catalytic efficiency for decomposition of hydrogen peroxide among all iron oxide catalysts developed until now.

The difficult control of the phase composition, crystal structure, and particle size distribution of the final iron(III) oxide nanophases obtained by the oxidative decomposition routes is considered to be the main disadvantage. These are unambiguously related to a broad range of experimental parameters affecting the mechanism and kinetics of the solid-state oxidative reactions including the reaction temperature and time, reaction atmosphere (static air, dynamic air, oxygen stream, limited air conditions, water vapor atmosphere, etc.), precursor particle size and morphology, precursor layer thickness, and conditions for evolution and/or participation of the gaseous products (closed vs opened systems, gas outlet, etc.). Moreover, the polymorphous transformations of metastable polymorphs to hematite can have an indispensable impact on the final composition of samples. An exemplary system demonstrating the immense influence of the reaction conditions on the phase composition of the iron oxide nanophase is the thermally induced decomposition of iron(II) oxalate, where iron (α -Fe), iron carbide (Fe_3C), siderite (FeCO_3), wüstite (FeO), magnetite, and various Fe_2O_3 polymorphs appear in the mixtures of reaction products depending on the reaction atmosphere and other variables.^{43,45–51} Even in the nonreduction atmosphere, wüstite, magnetite, amorphous Fe_2O_3 , maghemite, and hematite can be produced from decomposition of iron(II) oxalate depending on the experimental conditions.

Nevertheless, two recent papers^{43,45} report on the possibility to control the crystal structure of iron oxide nanophase through the reaction conditions. Thus, Zhou at al. controlled the phase composition of the reaction products toward

magnetite, maghemite, and/or hematite single phases by varying the reaction atmosphere and temperature.⁴³ In our recent study we show that the surface area and crystal structure of nanoparticles between amorphous Fe_2O_3 and hematite can potentially be controlled by reaction time at a suitably set reaction temperature, which had an enormous impact on the catalytic efficiency of as-prepared nanopowders.⁴⁵ In the present paper we report on a unique opportunity to control the crystal structure of iron(III) oxide nanoparticles from oxidative solid-state decompositions of iron(II) salts through the powder layer thickness in the same reaction atmosphere, set reaction temperature, and precursor characteristics. We introduce the term “critical sample layer thickness (weight)” in the solid-state chemistry as this variable has a crucial impact on the heat effects, mechanism, and kinetics of oxidative decompositions and consequently on the crystal structure of the oxidic products. The dramatic time-limited increase of temperature observed during oxidative decompositions of samples above the critical weight represents a general phenomenon, which we prove by several examples including different metal salts, and is most likely responsible for the literature discrepancies concerning the chemical composition and crystal structure of reaction products.

2. Experimental Section

2.1. Sample Preparation. Before the thermal treatment, $\text{FeC}_2\text{O}_4 \cdot 2\text{H}_2\text{O}$ powder (Sigma-Aldrich) was finely homogenized in an agate mortar. Samples of different weights were isothermally treated in a ceramic crucible (bottom diameter ca. 23 mm, volume 7.26 mL) inside a laboratory muffle furnace (LM 112.07, Linn High Therm GmbH) at a set temperature of 175 °C. Sample temperature (T_s) was continually monitored by Ni–Cr–Ni thermocouples (GTT101000, Greisinger electronic GmbH), which were in direct contact with the sample, and recorded using a digital multimeter (M-3850D, Metex Instruments) connected to a PC.

2.2. Sample Characterization. The transmission ^{57}Fe Mössbauer spectra of 512 channels were collected using a Mössbauer spectrometer at constant acceleration mode with a $^{57}\text{Co}(\text{Rh})$ source. Basic measurements were carried out at room temperature (RT). Low-temperature in-field Mössbauer spectra used for characterization of nanoparticles in superparamagnetic state were recorded at 5 K in an external magnetic field of 8 T, applied parallel to the propagation of γ -rays, using a cryomagnetic Oxford Instruments system. The isomer shift values were referred to α -Fe at RT. An X'Pert PRO instrument with $\text{Co K}\alpha$ radiation was employed for XRD (X-ray powder diffraction) analyses. Phase composition of the samples was evaluated using an X'Pert HighScorePlus software package (PANanalytical) and the JCPDS PDF-4 database. Transmission electron microscopy images (TEM) were obtained on the JEOL JEM 2010 microscope operated at 200 kV (LaB₆ cathode, point-to-point resolution 1.94 Å). The pictures were collected by the CCD camera KeenView with resolution of 1392 × 1040 pixels using the ITEM software package. Sample material was disintegrated in ethanol solution by ultrasound. The suspension was placed on copper grid coated by holey carbon. The ethanol was dried out by evaporation at ambient temperature. A superconducting quantum interference device (SQUID, MPMS XL-7, Quantum Design) was used for the magnetic measurements. The hysteresis loops were collected at 2 and 300 K in external magnetic fields from –70 to +70 kOe.

(43) Zhou, W. W.; Tang, K. B.; Zeng, S. A.; Qi, Y. X. *Nanotechnology* **2008**, *19*, 065602.

(44) Piao, Y.; Kim, J.; Bin Na, H.; Kim, D.; Baek, J. S.; Ko, M. K.; Lee, J. H.; Shokouhimehr, M.; Hyeon, T. *Nat. Mater.* **2008**, *7*, 242–247.

(45) Hermanek, M.; Zboril, R.; Medrik, I.; Pechousek, J.; Gregor, C. *J. Am. Chem. Soc.* **2007**, *129*, 10929–10936.

(46) Carles, V.; Alphonse, P.; Tailhades, P.; Rousset, A. *Thermochim. Acta* **1999**, *334*, 107–113.

(47) McCollom, T. M.; Simoneit, B. *Origins Life Evol. Biosphere* **1999**, *29*, 167–186.

(48) Gabal, M. A.; El-Bellihi, A. A.; Ata-Allah, S. S. *Mater. Chem. Phys.* **2003**, *81*, 84–92.

(49) Hermanek, M.; Zboril, R.; Mashlan, M.; Machala, L.; Schneeweiss, O. *J. Mater. Chem.* **2006**, *16*, 1273–1280.

(50) Ganguli, A. K.; Ahmad, T. *J. Nanosci. Nanotechnol.* **2007**, *7*, 2029–2035.

(51) Hakim, L. F.; Vaughn, C. L.; Dunsheath, H. J.; Carney, C. S.; Liang, X.; Li, P.; Weimer, A. W. *Nanotechnology* **2007**, *18*, 345603.

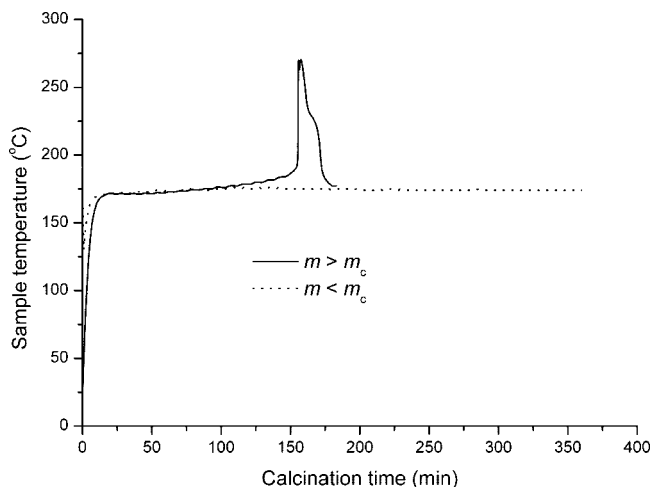


Figure 1. Temperature records of the samples below (dotted line) and above a critical weight m_c (solid line) taken during the isothermal treatment of $\text{FeC}_2\text{O}_4 \cdot 2\text{H}_2\text{O}$ at the set furnace temperature of $T = 175^\circ\text{C}$.

3. Results and Discussion

3.1. Effect of the Sample Layer Thickness: Isothermal versus Nonisothermal Treatment. Precise measurement of the sample temperature has proved to be a breaking point allowing the monitoring of the remarkable effect of the powder layer thickness on the decomposition process of $\text{FeC}_2\text{O}_4 \cdot 2\text{H}_2\text{O}$ in air. As a result we observed specific thermal behavior of the samples during isothermal heating depending on their weights (representing different thicknesses of the powder samples in a given experimental geometry, i.e., the shape, diameter, and volume of the ceramic crucible). While below a certain sample mass (critical mass, m_c) the sample temperature (T_s) almost precisely followed the set furnace temperature (T), above it, T_s conspicuously increased at a certain moment and after a specific period of time (ca. 20 min) decreased back to T . This principal effect of the powder layer thickness is well demonstrated in Figure 1 showing the temperature records of two representative samples—one below (1 g) and one above (2.4 g) m_c . In a given geometry, for $T = 175^\circ\text{C}$, m_c turned to be ca. 1.6 g. The temperature record of the sample of $m > m_c$ (solid line) clearly demonstrates that in such a case the sample temperature can temporarily increase to more than 50% of the set temperature ($T_s = 270^\circ\text{C}$ vs $T = 175^\circ\text{C}$).

For simplicity, from this point onward we denominate this time-limited temperature increase as the “exoeffect” as it closely resembles exothermal effects accompanying oxidative decompositions and other heat-evolving processes observed in DTA (differential thermal analysis) and DSC (differential scanning calorimetry) curves during dynamic heating. The temperature profile during such an exoeffect proved to be dependent on the depth within the sample volume as shown in Figure 2. T_s was simultaneously measured in three different points by appropriately positioned thermocouples fixed to the crucible: (i) below the sample surface, (ii) at the bottom inside of the crucible, and (iii) at the bottom outside of the crucible. One can clearly visualize that until the exoeffect comes, the temperature records are almost the same ($\pm 2^\circ\text{C}$) indicating a very good temperature transfer within the whole sample volume. The first and most intensive thermal change

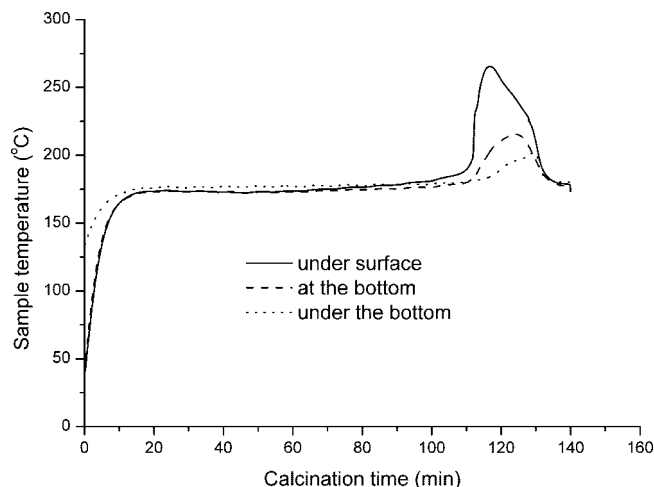


Figure 2. Dependence of the exoeffect on the position within the sample volume. Set furnace temperature $T = 175^\circ\text{C}$.

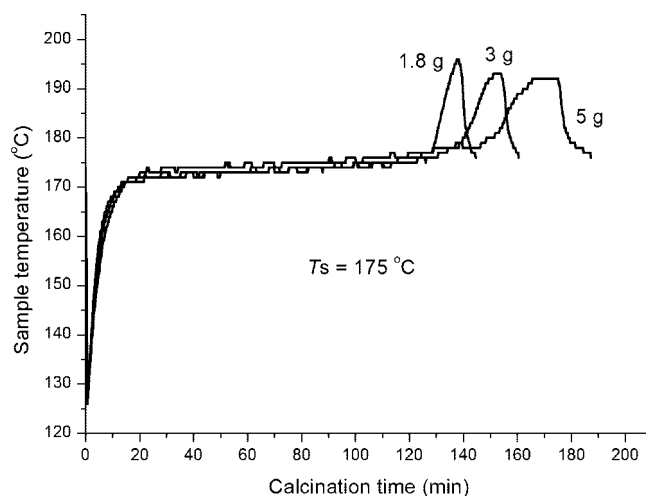


Figure 3. Dependence of the exoeffect on the sample mass. Set furnace temperature $T = 175^\circ\text{C}$. T_s recorded under the bottom of the crucible.

takes place in the subsurface layer (solid line). Toward the bottom (dashed and dotted lines, respectively) the exoeffects start later and the intensities are far lower. It undoubtedly indicates that the initiation of the exoeffect comes from the outside and proceeds into the sample volume and is therefore probably caused by penetrating air oxygen.

Figures 3 and 4 show the dependences of the exoeffect on the sample weight m at a constant T and on the set T at a constant m , respectively. It can be concluded that the exoeffect comes earlier the lower the sample mass and/or the higher the set temperature.

The presented data unambiguously reveal that the combination of the sample mass and set temperature have a profound impact on the thermal behavior of the sample and result generally in two different ways of decomposition of $\text{FeC}_2\text{O}_4 \cdot 2\text{H}_2\text{O}$ —one truly isothermal and the other denominated as “quasi-isothermal” in which the sample temperature temporarily exceeds the set temperature.

Hence, in the following sections two representative decomposition processes from the viewpoint of their temperature profile are discussed. We clearly show that these two examples lead to two completely different decomposition mechanisms (at the same set temperature) resulting in

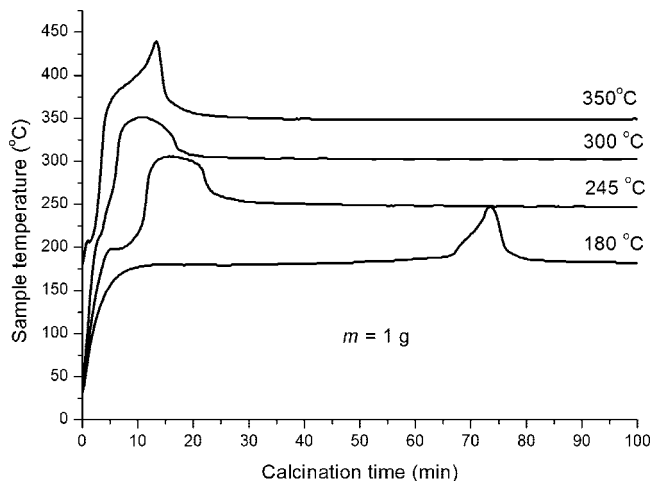


Figure 4. Dependence of the exoeffect on the set furnace temperature. Sample mass $m = 1$ g.

different polymorphous composition of the reaction products. We also provide an explanation for exoeffect initiation and demonstrate that it is a general phenomenon that should be seriously taken into account in all solid-state oxidation–decomposition reactions.

3.2. Mechanism and Kinetics of the “Quasi-Isothermal” Conversion. The decomposition mechanism at conditions below m_c is comprehensively discussed in our former publication,⁴⁵ where all related HRTEM (high-resolution transmission electron microscopy), Mössbauer, and XRD data can also be found. Briefly, 1 g of $\text{FeC}_2\text{O}_4 \cdot 2\text{H}_2\text{O}$ was chosen as a suitable weight below the critical mass representing the “truly isothermal process” where the sample temperature T_s followed precisely the set temperature T . At 175 °C the decomposition took place in two steps with the primary formation of amorphous Fe_2O_3 nanoparticles (2–3 nm) which consequently slowly crystallized toward thermally stable hematite at longer calcination times (ca. 13 nm after 100 h of the isothermal treatment). Except for hematite, no other polymorphs were detected among products during the reaction process.

As a representative mass of the samples exhibiting exothermal behavior and leading therefore to the “quasi-isothermal decomposition” during heating at 175 °C, we chose 2.4 g of $\text{FeC}_2\text{O}_4 \cdot 2\text{H}_2\text{O}$ (denoted as sample E). The phase composition was monitored by XRD and Mössbauer spectroscopy at different time points E_1 – E_6 up to the end of the exoeffect as shown in Figure 5. We also performed the phase analysis of the samples heated for additional 1, 25, 50, and 100 h after the exoeffect finished (samples E_7 – E_{10} , respectively). Representative Mössbauer spectra and corresponding XRD patterns (E_5 , E_6 , E_8 , and E_{10}) are shown in Figure 6; all obtained Mössbauer parameters are presented in Table 1. The time change in the phase composition of the sample reflecting both the mechanism and kinetics of the decomposition process is monitored by the dependence of the relative areas (RA) of the corresponding Mössbauer spectra on the calcination time (Figure 7).

Mössbauer spectra of samples E_1 – E_4 (not shown), reflecting the phase composition before the exoeffect starts, reveal only two doublet components. The one with hyperfine

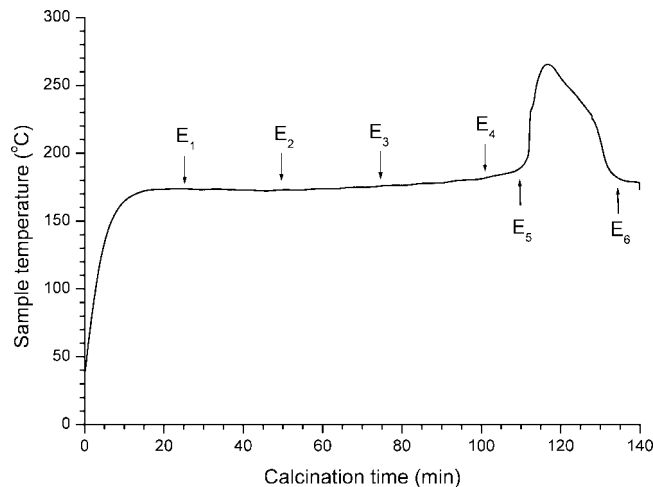


Figure 5. Time points at which the phase composition of the sample was analyzed ($m = 2.4$ g), heated at $T = 175$ °C in air.

parameters of $\delta = 1.18$ – 1.19 mm s^{-1} and $\Delta E_Q = 1.68$ – 1.70 mm s^{-1} clearly stands for Fe^{2+} in the ferrous oxalate structure. The second doublet ($\delta = 0.27$ – 0.33 mm s^{-1} and $\Delta E_Q = 0.80$ – 0.85 mm s^{-1}) represents highly distorted Fe^{3+} cations in the nascent superparamagnetic iron(III) oxide structure. It can be clearly seen that after 100 min of the isothermal treatment (E_4) the content of ferrous oxalate gradually decreased to 69% in favor of superparamagnetic Fe_2O_3 nanoparticles (31%).

Samples E_5 and E_6 are of key importance as they monitor the phase composition at the very beginning and exactly after the exoeffect, respectively. The sample temperature at the time corresponding to E_5 has already slightly exceeded the set 175 °C as seen in Figure 5. Its Mössbauer spectrum is qualitatively the same as that of the previous sample (E_4), the decrease in the oxalate content (from 69% to 52%) is, however, far steeper. The corresponding XRD pattern confirms that hydrated/anhydrous mixtures of $\text{FeC}_2\text{O}_4 \cdot 2\text{H}_2\text{O}$ / FeC_2O_4 are the only crystalline phases present in the sample. The fraction of superparamagnetic Fe_2O_3 nanoparticles observed in the Mössbauer spectrum is X-ray amorphous and therefore cannot be seen in the pattern.

The Mössbauer spectrum and XRD pattern of sample E_6 , reflecting the phase composition immediately after the exoeffect, show completely different character when compared to the beginning of the exoeffect (E_5). It should be emphasized that the time difference between E_5 and E_6 (duration of the exoeffect) is ca. 20 min which is only 14% of the overall decomposition time (i.e., up to E_6)! However, during such a short time interval, a depletion of almost all remaining ferrous oxalate occurs as its content decreased from 52% in E_5 to 4% in E_6 . Moreover, besides the residual oxalate and the superparamagnetic Fe^{3+} doublet, two magnetically split patterns (sextets) newly appear in the Mössbauer spectrum of sample E_6 . The sextet possessing 13% of the overall spectrum area with the hyperfine parameters of $\delta = 0.38$ mm s^{-1} , $\varepsilon_Q = -0.18$ mm s^{-1} , and $H = 48.0$ T can be clearly ascribed to weakly ferromagnetic hematite. On the other hand, the zero value of the quadrupole shift in the second less intensive sextet ($H = 42.5$ T) and the considerably lower isomer shift ($\delta = 0.32$ mm s^{-1}) allow

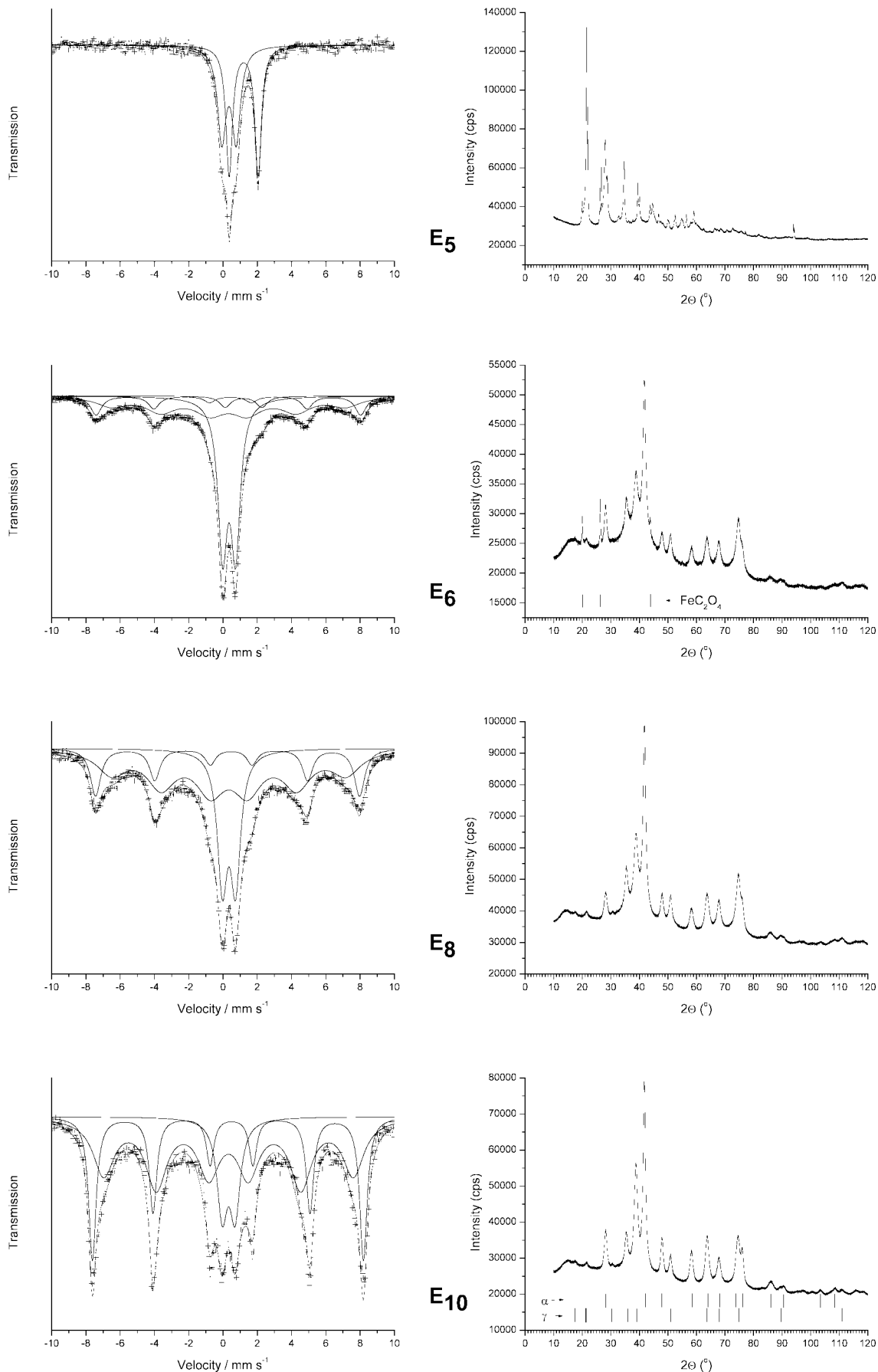


Figure 6. Representative RT Mössbauer spectra and corresponding XRD patterns of samples E₅, E₆, E₈, and E₁₀ prepared by quasi-isothermal decomposition of 2.4 g of FeC₂O₄·2H₂O at 175 °C. Samples were heated until the very beginning of the exoeffect (E₅), the very end of the exoeffect (E₆), and for 25 (E₈) and 100 h (E₁₀) after the exoeffect finished, respectively.

Table 1. Mössbauer Parameters of Samples E₁–E₁₀ Prepared by Quasi-Isenthal Decomposition of 2.4 g of FeC₂O₄·2H₂O at 175 °C for Different Periods of Time

sample	<i>t</i> ^a	<i>T</i> _{meas} ^b	δ (mm s ⁻¹) ^c	ΔE_Q (mm s ⁻¹) ^d	ε_Q (mm s ⁻¹) ^e	<i>H</i> (T) ^f	RA (%) ^g	site assignment
E ₁	25 min	RT	1.19	1.70			93	FeC ₂ O ₄
			0.27	0.80			7	SP Fe ₂ O ₃
E ₂	50 min	RT	1.19	1.70			88	FeC ₂ O ₄
			0.33	0.84			12	SP Fe ₂ O ₃
E ₃	75 min	RT	1.18	1.68			82	FeC ₂ O ₄
			0.30	0.87			18	SP Fe ₂ O ₃
E ₄	100 min	RT	1.18	1.68			69	FeC ₂ O ₄
			0.33	0.85			31	SP Fe ₂ O ₃
E ₅	the very beginning	RT	1.20	1.69			52	FeC ₂ O ₄
			0.35	0.84			48	SP Fe ₂ O ₃
E ₆	the very end of the EXO	RT	1.20	2.15			4	FeC ₂ O ₄
			0.36	0.77			45	SP Fe ₂ O ₃
			0.32		0	42.5	38	γ -Fe ₂ O ₃
			0.38		-0.18	48.0	13	α -Fe ₂ O ₃
E ₇	1 h after the EXO finished	RT	1.20	2.20			1	FeC ₂ O ₄
			0.36	0.77			41	SP Fe ₂ O ₃
			0.32		0	43.0	41	γ -Fe ₂ O ₃
			0.38		-0.21	48.5	17	α -Fe ₂ O ₃
E ₈	25 h after the EXO finished	RT	0.35	0.77			26	SP Fe ₂ O ₃
			0.34		0	42.5	55	γ -Fe ₂ O ₃
			0.37		-0.21	48.0	19	α -Fe ₂ O ₃
E ₉	50 h after the EXO finished	RT	0.34	0.76			19	SP Fe ₂ O ₃
			0.35		0	44.0	55	γ -Fe ₂ O ₃
			0.39		-0.21	48.0	26	α -Fe ₂ O ₃
E ₁₀	100 h after the EXO finished	RT	0.33	0.75			14	SP Fe ₂ O ₃
			0.32		0	45.0	55	γ -Fe ₂ O ₃
			0.39		-0.21	49.0	31	α -Fe ₂ O ₃

^a *t* = time of the thermal treatment at 175 °C. ^b *T*_{meas} = temperature at which the spectrum was recorded. ^c δ = isomer shift (with respect to metallic iron, ± 0.01). ^d ΔE_Q = quadrupole splitting (± 0.01). ^e ε_Q = quadrupole shift (± 0.01). ^f *H* = hyperfine magnetic field (± 0.5). ^g RA = relative spectrum area (± 1).

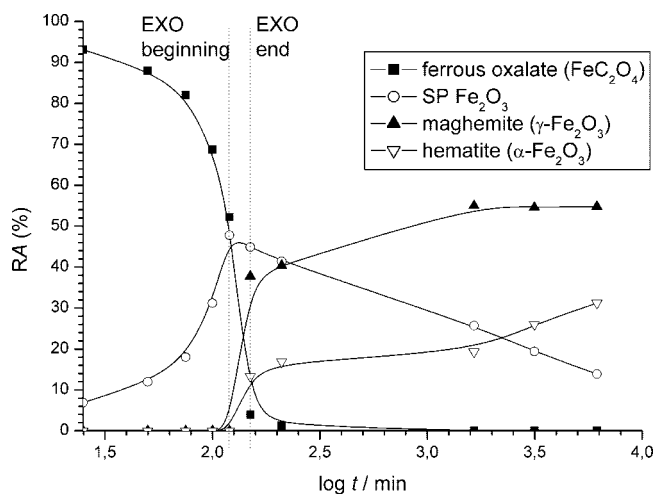


Figure 7. Time dependence of the relative spectrum areas (RA) as obtained from RT Mössbauer spectra of samples E₁–E₁₀ prepared by quasi-isothermal decomposition of 2.4 g of FeC₂O₄·2H₂O at 175 °C.

us to unambiguously identify this component as ferrimagnetic maghemite (38% of RA). Significantly reduced values of hyperfine magnetic fields of both sextets when compared to the values typical for well crystalline particles indicate very small particle dimensions of both compounds. Mössbauer observations are well supported by the corresponding XRD pattern (Figure 6). In addition to the minor remnants of the oxalate structure (marked in the pattern) clearly visible diffraction peaks belonging to cubic maghemite and hexagonal hematite structures appear. The relatively broad and overlapped lines indicate that particles of both structures are extremely small in volume.

Further changes in the phase composition, after the end of the exoeffect, were evaluated from samples E₇–E₁₀

(thermal treatments for 1, 25, 50, and 100 h after the exoeffect, respectively). The time dependence of the relative contents of individual phases (Figure 7) clearly shows that all essential events, including the violent decomposition of the substantial fraction of ferrous oxalate dihydrate and the simultaneous rapid formation of crystalline maghemite, have happened within ca. 20 min of the exoeffect duration. After the exoeffect, on the other hand, the system only slowly crystallizes as evidenced by the slow increase in the content of both crystalline maghemite and hematite at the expense of the ultrasmall superparamagnetic Fe₂O₃ fraction (see also the Mössbauer spectra and XRD patterns of samples E₈ and E₁₀ in Figure 6). Moreover, an increase in the content of hematite at longer calcination times (25–100 h) suggests the gradual particle size induced transformation of γ -Fe₂O₃ to α -Fe₂O₃.

To identify the structure of the ultrasmall superparamagnetic Fe₂O₃ nanoparticles arising as the primary decomposition product and to corroborate the suspected role of air oxygen as a trigger of the exoeffect we measured Mössbauer spectra of samples E₅ and E₆ (beginning and end of the exoeffect, respectively) at 5 K under the external magnetic field of 8 T applied parallel to the γ -ray propagation (the obtained samples are marked LE₅ and LE₆, respectively). These measuring conditions were chosen to unambiguously distinguish among ferrimagnetic maghemite, antiferromagnetic hematite, and superparamagnetic amorphous Fe₂O₃ structures which all could behave as indistinguishable superparamagnetics at RT. At such a low temperature (5 K) the average hyperfine magnetic field of the amorphous phase is significantly reduced when compared to magnetically ordered systems. Moreover, the second and fifth spectral lines of

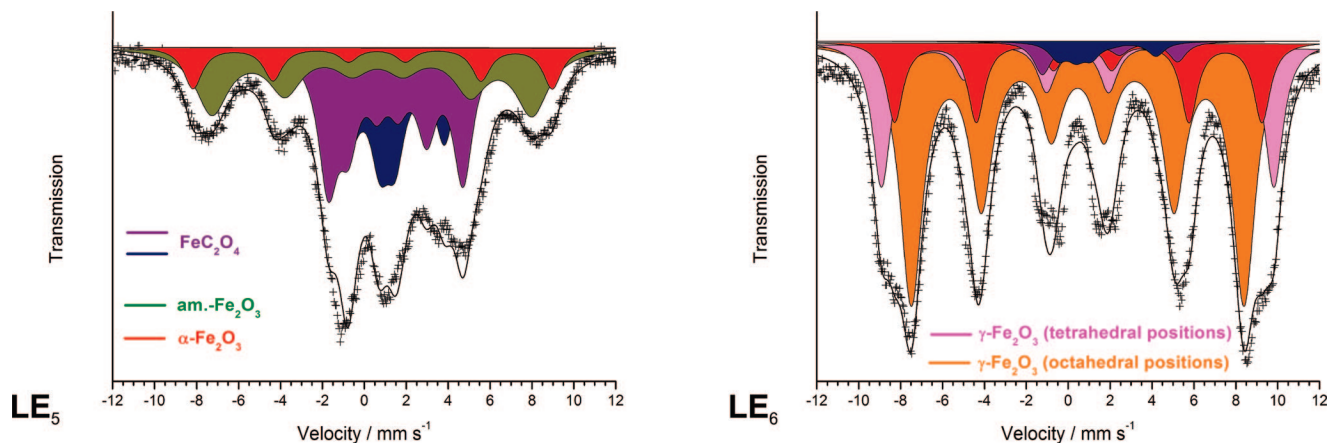


Figure 8. Low-temperature/in-field (5 K/8 T) Mössbauer spectra of samples E₅ (LE₅) and E₆ (LE₆).

Table 2. Mössbauer Parameters of Samples LE₅ and LE₆ Measured at 5 K under External Magnetic Field of 8 T

sample	t^a	T_{meas}^b	δ (mm s ⁻¹) ^c	ε_Q (mm s ⁻¹) ^e	H_{eff} (T) ^{f,g}	RA (%) ^h	site assignment
LE ₅	the very beginning of the EXO	5 K/8 T	1.30	0.39	14.5	26	FeC ₂ O ₄
			1.30	0.38	20.0	34	FeC ₂ O ₄
			0.50	-0.07	47.5	29	amorphous Fe ₂ O ₃
			0.50	-0.21	53.0	11	α-Fe ₂ O ₃
LE ₆	the very end of the EXO	5 K/8 T	1.30	1.12	14.5	3	FeC ₂ O ₄
			1.30	1.40	20.0	3	FeC ₂ O ₄
			0.48	-0.21	54.5	16	α-Fe ₂ O ₃
			0.45	0	58.0	21	tetrahedral γ-Fe ₂ O ₃
			0.45	0	49.5	57	octahedral γ-Fe ₂ O ₃

^a t = time of the thermal treatment at 175 °C. ^b T_{meas} = temperature at which the spectrum was recorded. ^c δ = isomer shift (with respect to metallic iron, ± 0.01). ^d ΔE_Q = quadrupole splitting (± 0.01). ^e ε_Q = quadrupole shift (± 0.01). ^f H_{eff} = effective magnetic field (± 0.5). ^g Effective magnetic field represents a vector sum of the external and hyperfine magnetic fields: $\vec{H}_{\text{eff}} = \vec{H}_{\text{ext}} + \vec{H}$. ^h RA = relative spectrum area (± 1).

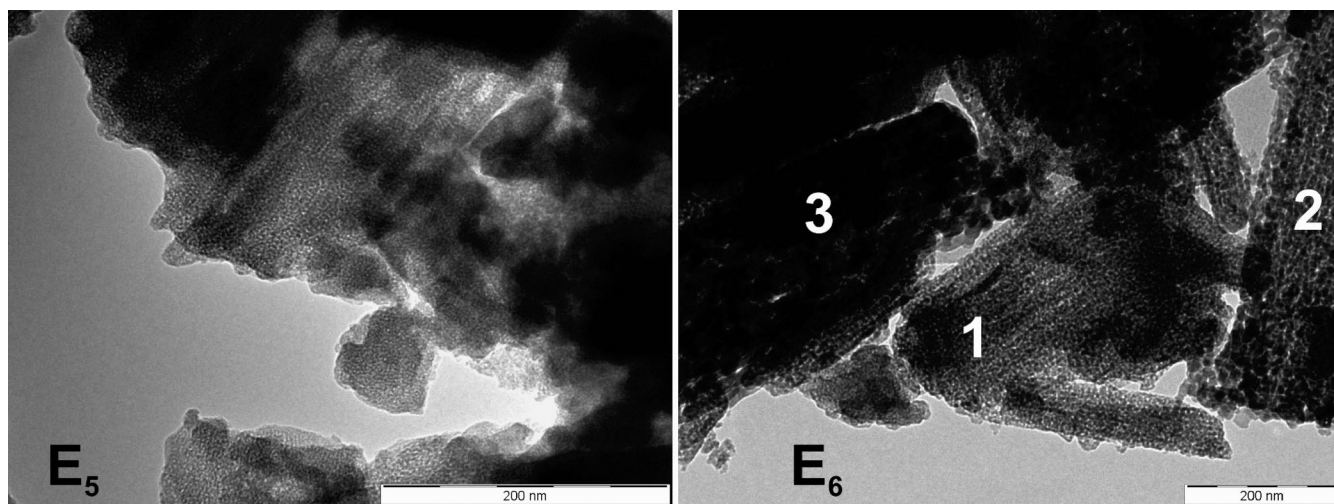


Figure 9. TEM images of samples E₅ (the very beginning of the exoeffect) and E₆ (the very end of the exoeffect): preferential orientation of the particles within the large platelike objects is observed. Nos. 1–3 in E₆ label three areas of different particle sizes: 5–6 nm (1), 7–12 nm (2), and 24–30 nm (3).

amorphous Fe₂O₃ do not reveal any change in their intensities (3:2:1:1:2:3) under external magnetic field.²⁹ On the other hand, the second and fifth spectral lines of hematite are noticeably enhanced (ideally 3:4:1:1:4:3) and those of maghemite suppressed (ideally 3:0:1:1:0:3) at the chosen measuring geometry as a result of their antiferromagnetic and ferrimagnetic behavior, respectively. In this case the particles are extremely small and/or preferentially orientated. So-called spin frustration resulting in not fully enhanced (hematite) or suppressed (maghemite) second and fifth spectral lines is observed.⁵² With an assumption of these

substantial differences reflecting diverse magnetic behavior of the compounds we fitted the obtained in-field Mössbauer spectra of samples E₅ and E₆ as shown in Figure 8 and Table 2.

The spectrum of sample LE₅ is well fitted with four sextets. Two of them (deep blue and purple colors) with significantly reduced hyperfine magnetic fields (14.5 and 20.0 T) and higher isomer shift of $\delta = 1.30$ mm s⁻¹ represent two different positions of Fe²⁺ in partially/fully dehydrated and

(52) Tucek, J.; Zboril, R.; Petridis, D. *J. Nanosci. Nanotechnol.* **2006**, *6*, 926–947.

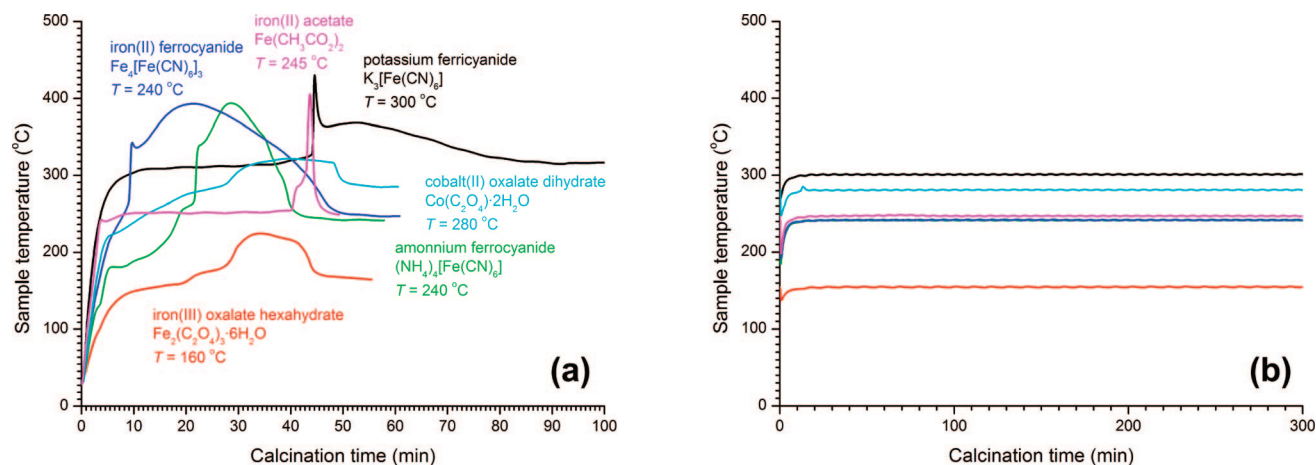


Figure 10. Temperature records of six different precursors exhibiting the exothermal behavior in the case when their sample mass exceeds m_c (a) and isothermal temperature profiles when their mass is below m_c (b).

still undecomposed ferrous oxalate (60% of RA). The other two sextets possess an isomer shift value ($\delta = 0.50 \text{ mm s}^{-1}$) typical for Fe^{3+} cations (including the temperature shift). The broader sextet (green) possessing a significantly lower value of hyperfine magnetic field (47.5 T) and unchanged spectral intensities of the second and fifth lines can be clearly ascribed to amorphous Fe_2O_3 . The second, much narrower Fe^{3+} sextet component (red) exhibiting much higher hyperfine magnetic field (53.0 T) with noticeably enhanced intensities of the second and fifth lines (3:2.4:1:1:2.4:3) can be assigned to hematite. A negative value of quadrupole shift (-0.21 mm s^{-1}) confirms its weakly ferromagnetic nature even at such low temperature (5 K)—which is far below the Morin transition temperature (260 K)—indicating that the size of the particles is smaller than 20 nm.¹ Such a small size in combination with a preferential orientation in a sample can cause the ratio of the spectral lines to differ from the ideal one. This observation is in a good agreement with the size and morphology of sample E_5 (Figure 9) appearing as large platelike objects composed of ultrasmall (3–4 nm in diameter) nanoparticles.

The in-field Mössbauer spectrum of sample E_6 (LE_6) fitted with five sextets exhibits only a minor contribution of the precursor (6%). The significantly heightened values of quadrupole shift (1.12 and 1.40 mm s^{-1}) when compared to sample LE_5 indicate higher distortion of the symmetry of the Fe^{2+} vicinity possibly resulting from a spike in sample temperature during the exoeffect. The increased value of the hyperfine magnetic field of the hematite sextet (54.5 T) together with higher ratio of the intensities of the second and fifth lines (3:3:1:1:3:3) indicates an increase in the particle size caused by the exoeffect temperature spike. The remaining two sextets possessing zero value of quadrupole shift with hyperfine magnetic fields of 58 and 49.5 T are typical for Fe^{3+} cations coordinated in the tetrahedral (pink) and octahedral (orange) positions in the maghemite structure, respectively. As the ideal ratio between tetrahedral and octahedral Fe^{3+} positions is 3/5, the actual ratio of 3/8 indicates that the structure is highly vacant. Significantly suppressed but nonzero values of the intensities of the second and fifth lines confirm, as in the case of hematite in LE_5 , nanoscopic particles with preferential orientation (see Figure

9). When compared to the TEM image of sample E_5 , however, there is a wide polydispersity in the particle sizes ranging from 5–6 nm (area 1), through 7–12 nm (area 2), up to 24–30 nm (area 3) reflecting different oxygen access/sample temperature conditions during the exoeffect resulting in formation of different iron(III) oxide structures (amorphous Fe_2O_3 , maghemite, hematite, respectively).

From the data presented in this study, it can be concluded that in the case of the high-layer sample (sample E , $m > m_c$), before the exoeffect occurs, ferrous oxalate in the (sub)surface layer, where the oxygen access is still sufficient, slowly decomposes to amorphous Fe_2O_3 (as evidenced in sample LE_5). So the decomposition proceeds in the same way as in the low-layer samples.⁴⁵ In spite of excellent temperature penetration through the whole sample volume (as proved in Figure 2) there is, however, no oxygen access into the deeper parts of the sample which undoubtedly prevents ferrous oxalate decomposition at 175 °C (verified by monitoring the phase composition at different depths of the sample volume—the deeper under the surface, the higher the content of the undecomposed precursor). With increasing calcination time, however, the (sub)surface powder layer becomes more porous enabling better penetration of air oxygen into the sample volume. The rate of the oxalate decomposition gradually increases (as is obvious in Figure 7), and at a certain moment (E_5 , the very beginning of the exoeffect) progressively penetrating oxygen abruptly ignites the preheated and still undecomposed remains of the precursor in the deeper parts of the crucible (52% of RA in E_5). This causes the abrupt and massive increase in the sample temperature lasting for ca. 20 min (Figure 5). Hence, within this relatively short time interval the remaining amount of FeC_2O_4 decomposes under completely different conditions (steep temperature gradient with a maximum at 265 °C causing the time-limited acceleration of the reaction kinetics, insufficient and not fluent access of air oxygen) when compared to ca. 120 min of the “ideal” isothermal decomposition before the exoeffect.⁴⁵ These “extreme” conditions can therefore unambiguously explain the formation of the vacant and thermally unstable structure of maghemite, which was present only after exoeffect totaling 78% (38% in

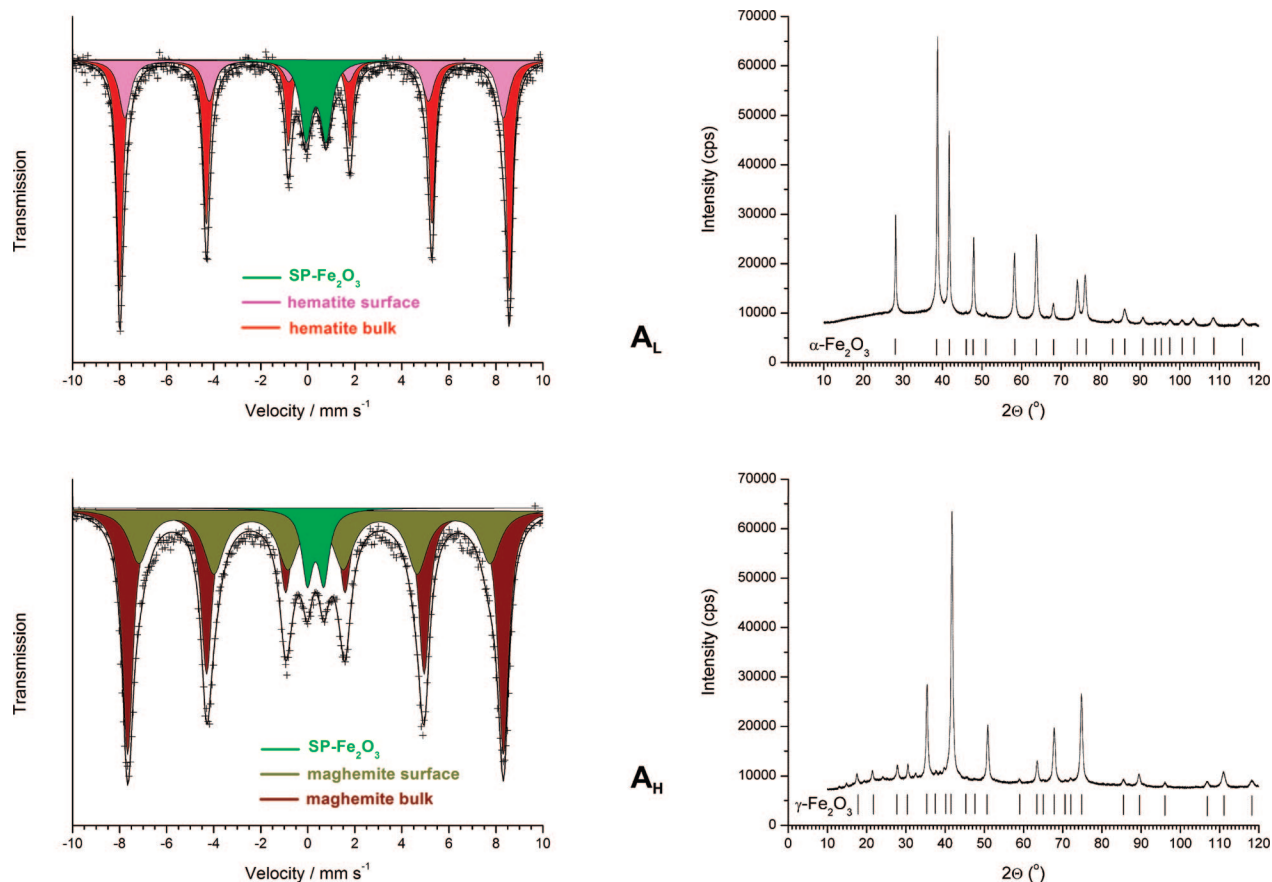


Figure 11. RT Mössbauer spectra and XRD patterns of iron(III) oxide prepared from iron(II) acetate: A_L (50 mg, $T = 245\text{ °C}$, 16 h) and A_H (500 mg, $T = 245\text{ °C}$, behind the exoeffect; 50 min, $T_{\text{MAX}} = 404\text{ °C}$).

Table 3. RT Mössbauer Parameters of Samples Prepared from Iron(II) Acetate Powders Differing in Masses (A_L, 50 mg, versus A_H, 500 mg)

sample	t (h) ^a	T_{meas} ^b	δ (mm s ⁻¹) ^c	ΔE_Q (mm s ⁻¹) ^d	ε_Q (mm s ⁻¹) ^e	H (T) ^f	RA (%) ^g	site assignment
A _L	16	RT	0.35	0.86	-0.19	51.5	16	SP-Fe ₂ O ₃
			0.38				58	α-Fe ₂ O ₃ bulk
			0.37				26	α-Fe ₂ O ₃ surface
A _H	behind the exoeffect (ca. 50 min)	RT	0.33	0.70	0	49.5	8	SP-Fe ₂ O ₃
			0.33				56	γ-Fe ₂ O ₃ bulk
			0.31				36	γ-Fe ₂ O ₃ surface

^a t = time of the thermal treatment at 245 °C. ^b T_{meas} = temperature at which the spectrum was recorded. ^c δ = isomer shift (with respect to metallic iron, ± 0.01). ^d ΔE_Q = quadrupole splitting (± 0.01). ^e ε_Q = quadrupole shift (± 0.01). ^f H = hyperfine magnetic field (± 0.5). ^g RA = relative spectrum area (± 1); SP = superparamagnetic fraction.

ferrimagnetic state and 40% in superparamagnetic form as concluded from E₆ and LE₆, respectively).

After the exoeffect, when the sample temperature is again stabilized at the set temperature, there is a slow relaxation process with increasing calcination time (Figure 7) and the particle size induced transformation $\gamma\text{-Fe}_2\text{O}_3 \rightarrow \alpha\text{-Fe}_2\text{O}_3$ is taking place.

It can therefore be concluded that good oxidative conditions in the narrow sample layer induce a truly isothermal process with thermally stable and structurally ideal (Fe³⁺ in only octahedral coordination, no vacancies) hematite as the only decomposition product. In worsened oxidation conditions the higher sample layer thickness yields a thermally unstable and vacant maghemite structure with two Fe³⁺ coordinations. The amount of maghemite in the sample strictly depends on how quickly the exoeffect comes. This situation is well depicted in Figure 4. The air access is the same for all samples (sample weight of 1 g in the same geometry), but the exothermal reaction proceeds earlier with

increasing set temperature. As a consequence, we observed various ratios of the maghemite/hematite mixtures, but the content of maghemite significantly increased at the expense of hematite with increasing set temperature. In other words, the earlier the time the exothermal reaction took place (the more quickly the decomposition was finished) the higher the content of maghemite was observed.

Hence, on the basis of discussed results we conclude specific conditions (an advantageous combination of the sample layer thickness and the set temperature) forming strictly monophasic products can be found. Indeed, the possibility of controlled syntheses leading to the desired products together with the generalization of observed phenomena from the viewpoint of other solid-state oxidative decomposition processes is demonstrated in the following section.

3.3. Generalization and Exploitation of the Results for the Controlled Syntheses. To illustrate that the above-described extraordinary effect of the powder layer thickness

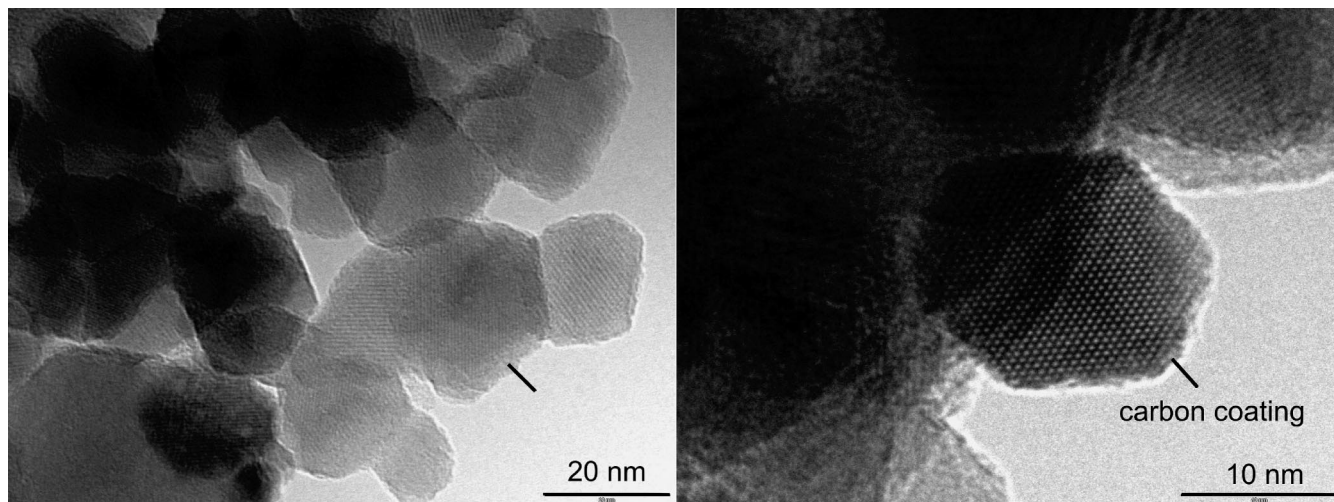


Figure 12. TEM image of exclusively maghemite nanoparticles prepared from iron(II) acetate at 245 °C in conditions above m_c (sample A_H).

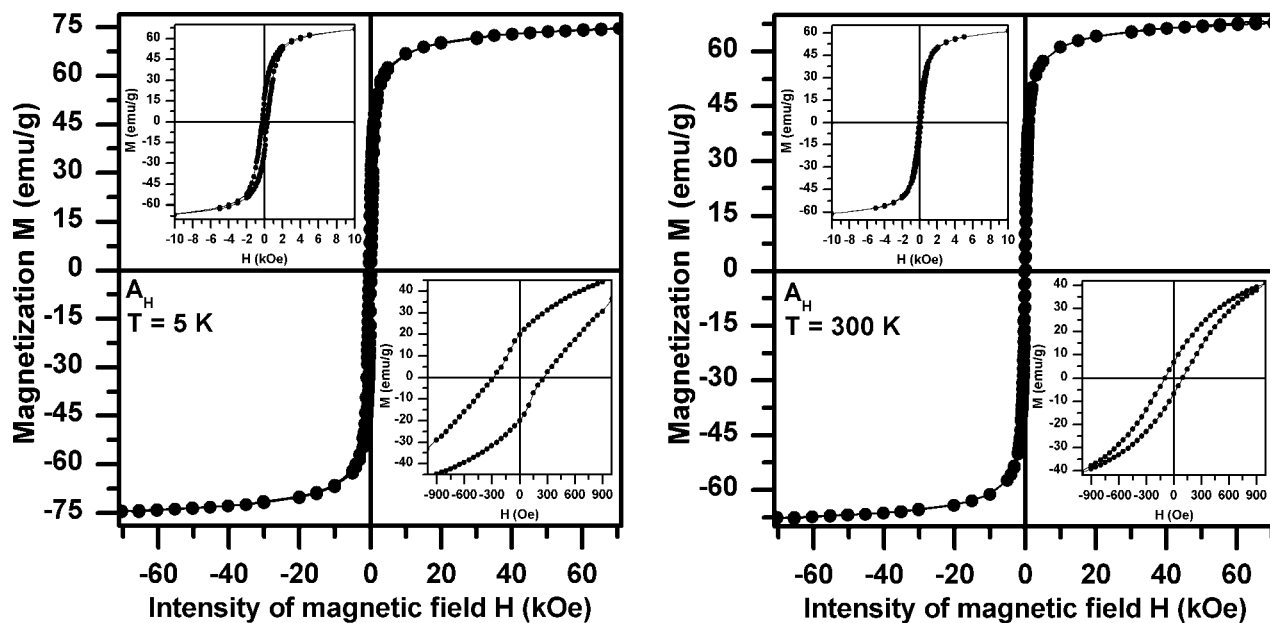


Figure 13. Hysteresis loops taken at 5 and 300 K for maghemite nanoparticles prepared from iron(II) acetate at 245 °C in conditions above m_c (sample A_H).

has a general relevance and therefore influences the mechanism of all oxidative decomposition processes we varied the powder thickness of six other compounds decomposing in the static air conditions at different set temperatures. The tested group of metal salts included potassium ferricyanide, $K_3[Fe(CN)_6]$ ($T = 300$ °C), iron(III) oxalate hexahydrate, $Fe_2(C_2O_4)_3 \cdot 6H_2O$ ($T = 160$ °C), ammonium ferrocyanide, $(NH_4)_4[Fe(CN)_6]$ ($T = 240$ °C), iron(III) ferrocyanide, $Fe_4[Fe(CN)_6]_3$ ($T = 240$ °C), cobalt(II) oxalate dihydrate, $CoC_2O_4 \cdot 2H_2O$ ($T = 280$ °C), and iron(II) acetate dihydrate, $Fe(CH_3CO_2)_2 \cdot 2H_2O$ ($T = 245$ °C). From the qualitative point of view the same results as for ferrous oxalate dihydrate were obtained, i.e., we observed a temporary significant increase in the sample temperature for powders with weights higher than m_c (above critical layer thickness), while the temperature profile corresponded well to the set furnace temperature below m_c (see Figure 10).

It is worth mentioning that the observed exoeffects need not necessarily be related to the oxidation of metals as

documented by examples of potassium ferricyanide and iron(III) oxalate, when the heat evolution and temporary increase in temperature are induced by oxidation of organic groups in a gaseous phase. Thus, the described phenomena relate to the large scale of metal salts with different oxidation states of metals. Similarly, the variation in the phase composition of metal oxides depending on the sample layer thickness must not be limited only to two polymorphs as documented by the above-mentioned example of hematite and maghemite formation during oxidative decomposition of iron(II) oxalate. Hence, we observed a preferential formation of the cubic “bixbyite-like” β - Fe_2O_3 structure from thermally induced oxidative conversion of Prussian blue ($Fe_4[Fe(CN)_6]_3$) in conditions of a narrow sample layer (1 mm), whereas maghemite turned to be a significantly prevailing phase in the thick-layer (4 mm) samples.⁴¹

The fundamental impact of the different diffusion conditions (caused by the varying sample layer thickness) on the phase composition of the products of oxidative decomposi-

tions in a solid state is illustrated with an example of iron(II) acetate. We clearly demonstrate that controlling the sample layer thickness can be a unique way toward syntheses of pure polymorphs possessing required structure. We isothermally heated two samples differing in powder masses (low-layer A_L , 50 mg, vs high-layer A_H , 500 mg, at the same geometry) at the same set temperature of 245 °C. As expected we observed two different decomposition processes (isothermal vs quasi-isothermal) resulting in pure hematite (A_L) and pure maghemite (A_H) samples, respectively. The obtained results are shown in Figure 11 and Table 3 presenting the RT Mössbauer data and corresponding XRD patterns.

From the presented results it is obvious that, when the key parameters are precisely controlled, single-phase nanocrystalline reaction products can be obtained. This can be extensively exploited to the syntheses of advanced materials possessing superior properties for a broad scale of applications. For example, in our previous study⁴⁵ we successfully prepared a heterogeneous hematite-based catalyst extraordinarily efficient in H_2O_2 degradation. Precise controlling of the sample layer thickness of $FeC_2O_4 \cdot 2H_2O$ below m_c and the low decomposition temperature allowed us to prepare nanomaterial with a unique combination of surface area and particle crystallinity resulting in the highest rate constant so far published for H_2O_2 degradation using environmentally friendly catalysts. On the other hand, if the sample mass is set above m_c , pure nanocrystalline maghemite can be synthesized as demonstrated with the example of an analo-

gous organic precursor—iron(II) acetate. As-prepared particles exhibit a perfect crystallinity, well-defined cubic morphology, and relatively narrow size distribution (see the TEM in Figure 12) related probably to the short time of the exoeffect duration (ca. 10 min., see Figure 10a). Moreover, the particles are well capped with the narrow layer of amorphous carbon formed on the maghemite surface during synthesis. Thus, this controlled oxidative decomposition represents an elegant one-step approach toward magnetic “core–shell” nanoparticles. The biocompatible character of the shell and suitable magnetic properties of the cores, including a high saturation magnetization achievable at low applied fields (see Figure 13), make the particles attractive for applications in various biomedical fields. Obviously, these solid-state routes controlled through the powder layer open the doors for the simple and cost-effective syntheses of advanced metal oxide-based nanomaterials, which can be used in a large scale of catalytic, magnetic, and biomagnetic applications.

Acknowledgment. This work has been supported by the Projects of the Ministry of Education of the Czech Republic (1M6198959201 and MSM6198959218) and the Academy of Sciences of the Czech Republic (KAN115600801 and KAN200380801). We warmly thank Yekaterina Krasnova from the Faculty of Chemistry, Florida Institute of Technology, Florida, for proof reading.

CM8011827